

NeuraLeaf: Neural Parametric Leaf Models with Shape and Deformation Disentanglement

Yang Yang¹ Dongni Mao¹ Hiroaki Santo¹ Yasuyuki Matsushita^{1,2} Fumio Okura¹

¹The University of Osaka ²Microsoft Research Asia – Tokyo

{yang.yang,mao.dongni,santo.hiroaki,yasumat,okura}@ist.osaka-u.ac.jp

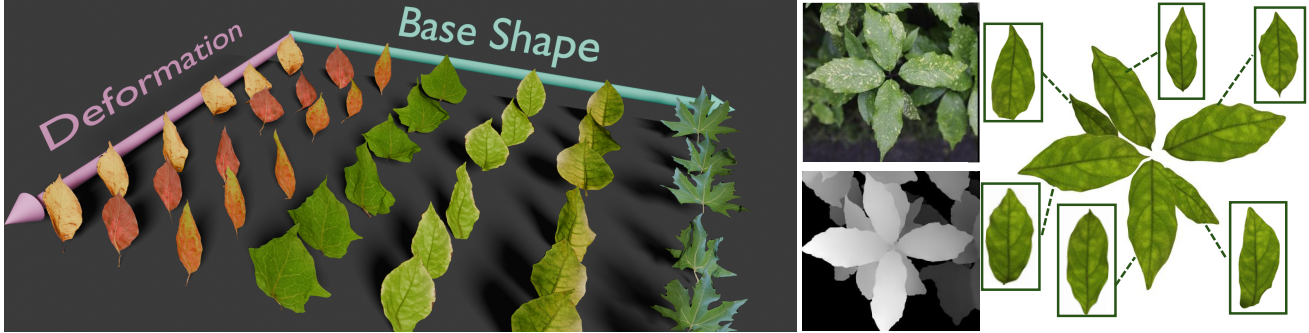


Figure 1. Our neural parametric model for leaves, NeuraLeaf, represents **shapes of various leaf species** and **natural 3D deformation**. Our model represents the leaves’ flattened shape and their 3D deformation in disentangled latent spaces (left). Our method enables the instance-wise reconstruction of leaves via fitting to real-world observations, besides pure CG modeling (right).

Abstract

We develop a neural parametric model for 3D leaves for plant modeling and reconstruction that are essential for agriculture and computer graphics. While neural parametric models are actively studied for humans and animals, plant leaves present unique challenges due to their diverse shapes and flexible deformation. To this problem, we introduce a neural parametric model for leaves, NeuraLeaf. Capitalizing on the fact that flattened leaf shapes can be approximated as a 2D plane, NeuraLeaf disentangles the leaves’ geometry into their 2D base shapes and 3D deformations. This representation allows learning from rich sources of 2D leaf image datasets for the base shapes, and also has the advantage of simultaneously learning textures aligned with the geometry. To model the 3D deformation, we propose a novel skeleton-free skinning model and create a newly captured 3D leaf dataset called DeformLeaf. We show that NeuraLeaf successfully generates a wide range of leaf shapes with deformation, resulting in accurate model fitting to 3D observations like depth maps and point clouds. Our implementation and dataset are available at <https://neuraleaf-yang.github.io/>.

1. Introduction

3D leaf reconstruction is important as it provides insights into plant growth in agricultural applications and is essen-

tial for creating virtual computer graphics (CG) assets. For domain-specific 3D shape reconstruction, parametric 3D models have shown remarkable success, such as for human bodies (e.g., SMPL [23]), animals (e.g., SMAL [59]), and even plant leaves [3, 5]. Although for modeling static leaves, some methods take bio-inspired approaches [42, 51] using venation patterns or the nature of flattened shapes.

Neural parametric models (NPMs) learn the mapping between latent codes and target shapes [11, 29, 31, 33, 50], showing their ability to represent detailed geometry for humans [7, 11, 33, 34, 37] trained from large-scale human canonical shapes and their deformations. However, the requirement of large datasets for training NPMs poses challenges for leaf modeling due to the lack of a 3D dataset containing leaves’ deformations.

To these issues, we integrate leaves’ bio-inspired insights with a data-driven framework. We propose a leaf-specific NPM representation, NeuraLeaf, leveraging the nature of leaves, i.e., the flattened leaves can be approximated as a plane. As illustrated in Fig. 1, we disentangle the leaves’ 3D geometry into their 2D base (i.e., flattened) shape and 3D deformation represented by different latent codes.

2D base shapes can be learned from 2D-scanned image datasets of leaves, often collected in biological studies (e.g., [44], [18]), mitigating the lack of a large-scale 3D leaf dataset. The 2D representation offers a natural and detailed shape representation while simplifying texture modeling by

treating the leaves’ textures as ordinary UV maps, casting the texture generation task to an image-to-image translation task from mask image to leaf UV texture.

For the 3D deformation modeling, we newly construct a dataset, DeformLeaf, by acquiring real-world 3D leaf shapes in natural deformation. This dataset consists of 3D-scanned leaf shapes along with their corresponding 2D shapes in a flattened state. This is the first 3D leaf dataset focused on leaf deformation modeling, including approximately 300 2D-3D leaf pairs, including complex deformations and detailed geometric features like venation. Since there still remains a gap between the scale of the 2D leaf image datasets and our DeformLeaf due to the practical limitations in acquiring diverse 3D scans of leaves, we further introduce novel regularization to ensure shape consistency.

Beyond data limitations, leaf deformation also presents challenges due to its high flexibility, and shape variance across species further complicates defining a common skeleton structure, making conventional skinned vertex-based models [6, 21, 28, 34, 48, 52, 53, 55] unsuitable. We, therefore, newly introduce a skeleton-free skinning model that learns a parametric space for skinning parameters. Specifically, we define a set of control points on a base plane to deform the leaf surface via transformation matrices based on skinning weights, associating any leaves to a unified deformation space. The shape latent controls both the base shape and skinning weights, while the deformation latent predicts rigid transformations for each control point. We use far more control points than usual NPMs for articulated objects like humans; this is a new direction of parametric modeling of fine-grained and highly flexible deformations that are essential for accurate leaf modeling and better generalization across different leaf shapes.

We showcase applications of our NeuraLeaf for reconstruction and modeling purposes, where our method enables the *leaf-wise* reconstruction from the observation as shown in Fig. 1. The quantitative and qualitative experiments demonstrate NeuraLeaf outperforms existing traditional parametric modeling and NPMs.

Contributions The chief contributions of this paper are:

1. We propose a leaf-specific NPM, NeuraLeaf, using the disentangled shape and deformation representation, which exploits the characteristics of flattened leaves. The 2D base shape representation achieves effective training from existing large 2D image datasets.
2. We newly introduce a skeleton-free skinning model for leaves, designed with many control points to capture geometric details like venation. We disentangle skinning weights and transformation matrices into two latent spaces, forming a compact representation.
3. We present a novel 3D leaf dataset DeformLeaf, which includes collections of base shapes and deformed leaves with their dense correspondences.

2. Related Work

2.1. Parametric Models

Traditional parametric models Blanz *et al.* [4] propose an early attempt at a parametric model representing facial variations using a low-dimensional shape space extracted by principal component analysis (PCA). Along with the improvements in the 3D registration technique [46] and large-scale data capture [1, 49], parametric 3D models have emerged as a leading method to model domain-specific deformable 3D shapes. The parametric models are studied in wide fields like human bodies [1, 23], hands [40], animals [59], faces [22], and leaves [3, 5]. SMPL [23], a representative example of parametric human body models, combines a low-dimensional shape space with an articulated blend-skinned model and is used in various applications [25, 38, 47]. However, such skinned vertex-based models have limited resolution and have difficulty representing non-rigid surface deformations often seen in leaves.

Neural parametric models (NPMs) Recently, neural implicit representations have been actively studied. DeepSDF [35], for instance, employs a feed-forward network to predict SDF values based on query locations, conditional on a latent code. Building upon this, recent parametric models called NPMs represent the dynamic nature of objects as well as their shape using neural networks [28, 32]. NPMs are mainly used for modeling human shape and deformation, in which we can access large-scale 3D datasets, such as for bodies [33, 34], faces [49], and heads [11].

2.2. Leaf Modeling

Parametric leaf modeling Traditionally, B-spline curves were used for representing silhouettes or veins of 2D leaves [19, 27], while they require tailor-made parameter sets for each group of leaves. For leaf modeling applicable to various leaves, Barley *et al.* [5] propose a parametric leaf model using a traditional PCA-based model [4] for leaf variation within a given flora species. Gaurav *et al.* [3] extend this direction for representation of non-planar leaves by using the Bezier curve, emphasizing identifying three pivotal features of leaf geometry: midrib, left/right silhouette, and the cross-section. However, PCA-based models are constrained by limited shape variability, lack deformation modeling, and require large 3D datasets. While offering parametric control of deformation, Bezier curve-based models still cannot capture the complex and natural deformations of real leaves. Compared to existing works, our work is the first to propose NPMs for leaves, representing natural and diverse shapes and deformation.

Leaf deformation modeling Existing methods for leaf deformation modeling often derive from physically-based simulations based on mesh. For instance, venation skeletons and surface membranes are used to model aging leaves

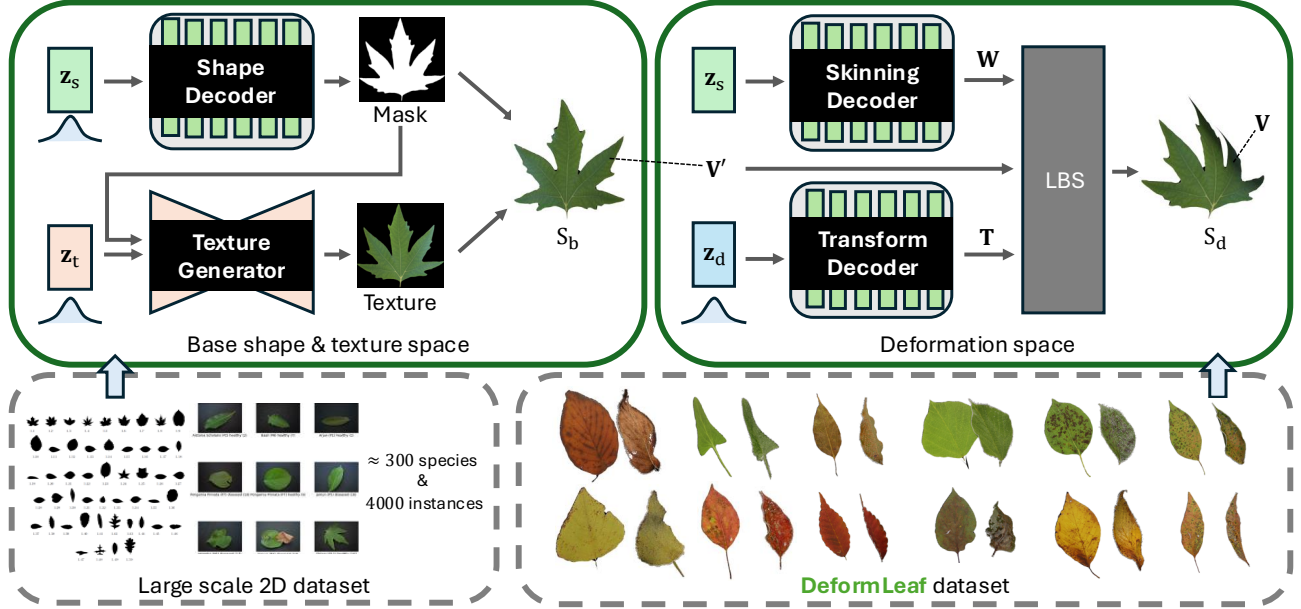


Figure 2. **Overview of NeuroLeaf.** We first learn the 2D base shape of leaves from a large-scale 2D dataset [9]. The base shape and texture spaces are modeled by a shape decoder f_{θ_s} and texture generator f_{θ_t} conditioned on shape & texture latent codes $\{z_s, z_t\}$. Based on the learned shape space, we then train two deformation decoders to predict skinning parameters, called skinning weight decoder f_{θ_w} and transformation decoder f_{θ_d} , which infer skinning weight of each point and transformation of each control point. We use linear blend skinning (LBS) [17] to deform the points. We learn the deformation space from our **DeformLeaf** dataset containing natural deformation.

[14], allowing for interactive user-driven deformation. Similarly, [24] introduces a technique to animate leaf wilting due to gravity, also employing a venation skeleton for deformation. Jeong *et al.* [45] generate intricate wrinkles and folds in leaves by simulating inhomogeneous shrinkage, which is influenced by physical properties like loss of water. Beyond those limited variations of deformations, our approach learns an implicit representation of deformation directly from real scanned leaf data, enabling high-fidelity and general-purpose modeling and reconstruction.

Bio-inspired leaf modeling Although static, a bio-inspired approach [51] reconstructs leaf shape using a hierarchical manner using the venation and margin information. Similarly, [42] generates leaves’ venation patterns using leaf-specific rule sets. Our method aims to leverage the leaves’ characteristics with data-driven NPMs.

3. NeuroLeaf: Neural Parametric Leaf Model

The overview of our disentangled representations and training strategy is illustrated in Fig. 2.

3.1. Shape Space

NeuroLeaf represents leaves’ base shape on a plane, enabling the training of the base shape space using large-scale 2D leaf image datasets. We use a hybrid representation combining a 2D signed distance function (SDF) for precise boundary modeling and meshes for better capability for downstream tasks.

Representation We first represent the base leaf shape in a flattened state using a neural SDF conditioned by a latent code. Given a latent code for a base shape (hereafter, referred to as shape latent code) $z_s \in \mathbb{R}^{N_s}$ as a condition, a multi-layer perceptron (MLP) for shape space (which we call the shape decoder f_{θ_s} maps a 2D base point $\mathbf{x} \in \mathbb{R}^2$ to its signed distance \tilde{d} from the surface of the base shape S_b^* , represented as the zero-level set of the shape MLP f_{θ_s} as

$$S_b^* = \{\mathbf{x} \in \mathbb{R}^2 \mid f_{\theta_s}(\mathbf{x}, z_s) = 0\}. \quad (1)$$

We then convert the SDF into a mask \mathbf{I}_m in a differentiable manner using the sigmoid function as

$$\mathbf{I}_m(\mathbf{x}) = \frac{1}{1 + e^{-k f_{\theta_s}(\mathbf{x})}}, \quad (2)$$

where k is learnable to control the slope. We then apply a threshold of 0.5 to obtain binary outputs and convert the pixels with the value 1 into vertices on the xy (*i.e.*, $z = 0$) plane. Finally, these vertices are triangulated to construct the base mesh $S_b = (\mathcal{V}', \mathcal{F}')$, where $\mathcal{V}' = \{\mathbf{v}'_i \in \mathbb{R}^3\}$ denotes the vertices and \mathcal{F}' denotes a set of face indices.

Training Thanks to the base shape spanning a plane, we can train the shape MLP f_{θ_s} using existing 2D leaf scan datasets such as [9] shown in Fig. 2. Since the 2D scans are acquired at a controlled setup, these are straightforwardly converted to 2D silhouettes by off-the-shelf segmentation models (*e.g.*, [20]), providing the ground-truth shape for

training. Once the ground-truth shape is obtained, we follow the common training strategy of neural implicit representations. Specifically, we sample points from a unit 2D grid along with SDF values to compute the loss functions. SDF loss \mathcal{L}_{sdf} evaluates ℓ_1 loss between the predicted SDF \tilde{d} and the ground-truth SDF d as

$$\mathcal{L}_{\text{sdf}} = \|\tau(\tilde{d}, \delta_\tau) - \tau(d, \delta_\tau)\|_1, \quad (3)$$

where $\tau(d, \delta) := \min(\delta_\tau, \max(-\delta_\tau, d))$ is a truncation function controlled by δ_τ to disregard the large SDF values. We compute the ℓ_1 loss for both predicted SDF and resulting mask. This helps in effectively learning the differentiable conversion from SDF to mask while ensuring that the mask closely aligns with the ground-truth silhouette. We also introduce the Eikonal regularizer [13] \mathcal{L}_{eik} to ensure the gradient norm of the SDF approximates. Furthermore, similar to [33], we apply a latent regularization term \mathcal{L}_{lat} , with which the shape latent codes are constrained to follow a zero-mean multivariate Gaussian distribution, using a spherical covariance defined by σ_s as

$$\mathcal{L}_{\text{lat}} = \frac{1}{\sigma_s^2} \|\mathbf{z}_s\|_2^2. \quad (4)$$

We minimize the loss over all S training samples to yield the shape latent codes $\{\mathbf{z}_s^i\}_{i=1}^S$, k , and MLP weights θ_s as

$$\operatorname{argmin}_{\theta_s, k, \{\mathbf{z}_s^i\}_{i=1}^S} \sum_{i=1}^S (\mathcal{L}_{\text{sdf}} + \mathcal{L}_{\text{sil}} + \mathcal{L}_{\text{eik}} + \mathcal{L}_{\text{lat}}). \quad (5)$$

3.2. Texture Space

Our texture space aims to represent the leaf’s appearance, aligning closely with its geometry, ensuring that the generated textures accurately correspond to the leaf’s base shape.

Representation We treat texture modeling as an image-to-image translation task so that an RGB image represents a texture map \mathbf{I}_t . Specifically, we use the CycleGAN [58] f_{θ_t} to map base mask \mathbf{I}_m to its corresponding texture map \mathbf{I}_t conditioned by a texture latent $\mathbf{z}_t \in \mathbb{R}^{N_t}$ as

$$\mathbf{I}_t = f_{\theta_t}(\mathbf{I}_m, \mathbf{z}_t). \quad (6)$$

Each pixel of \mathbf{I}_t corresponds directly to a vertex of the base mesh, allowing straightforward UV mapping to apply the texture onto the mesh.

Training We use the same datasets used in Sec 3.1 for training. Similar to [58], we use both GAN loss \mathcal{L}_{GAN} and cycle consistency loss \mathcal{L}_{cyc} .

3.3. Deformation Space

Deformation space represents the 3D deformation on the plane base mesh, trained using our DeformLeaf dataset containing base and deformed leaf shape pairs. We aim to learn a disentangled deformation parameter space where, given a deformation latent code, all samples, regardless of their shape, should exhibit a similar deformation pattern.

Representation Our neural blend skinning model depends on three key components: control points, skinning weights, and rigid transformation of each control point using linear blend skinning (LBS) [17]. We define K control points, noted as $\mathcal{C} = \{\mathbf{c}_k \in \mathbb{R}^3 \mid k = 1, \dots, K\}$, to control the deformation of each base mesh \mathcal{S}_b with N vertices in \mathcal{V}' , where N varies with different base shapes. To represent the complex and fine-grained deformations occurring on the diverse base shapes of leaves, we use a large number of control points compared to usual articulated objects like humans. Specifically, we set the maximum number of control points K to 1,000, which is distributed uniformly across the entire UV space.

The corresponding skinning weights are defined as $\mathcal{W} = \{w_{i,k} \mid i = 1, \dots, N, k = 1, \dots, K\}$, satisfying the condition where $0 \leq w_{i,k} \leq 1$ and $\sum_{k=1}^K w_{i,k} = 1$.

$$\tilde{\mathbf{v}}_i = \sum_{k=1}^K w_{i,k} \mathbf{T}_k(\tilde{\mathbf{v}}'_i - \tilde{\mathbf{c}}_k), \quad \forall \tilde{\mathbf{v}}'_i \in \mathcal{V}', \quad (7)$$

where tildes denotes their homogeneous form, e.g., $\tilde{\mathbf{v}}_i = [\mathbf{v}_i, 1]^\top$. We finally get the deformed shape $\mathcal{S}_d = (\mathcal{V}, \mathcal{F}')$, where \mathcal{F}' are the same set of faces as in the base shape \mathcal{S}_b .

Transformation decoder: The purpose of the transformation decoder f_{θ_d} is to predict the rigid transformation for each control point, represented by a quaternion. Unlike previous NPMs, which predict displacement conditioned on both shape and deformation latent codes, our approach aims to learn a disentangled deformation space independent of the shape. Therefore, we condition only on the deformation latent code $\mathbf{z}_d \in \mathbb{R}^{N_d}$ as

$$\mathcal{T} = f_{\theta_d}(\mathbf{z}_d, \mathcal{C}). \quad (8)$$

Skinning weights decoder: Given a base mesh \mathcal{S}_b with its shape latent code \mathbf{z}_s , the skinning weights decoder f_{θ_w} aims to predict the skinning weights \mathcal{W} corresponding to the control points. To ensure the deformation is adapted to each specific leaf shape, the mapping is defined as

$$\mathcal{W} = f_{\theta_w}(\mathbf{z}_s, \mathcal{V}'), \quad (9)$$

where \mathbf{z}_s serves as a global feature that links the skinning weights to the specific base shape.

Training The training process in the deformation space is divided into two stages to ensure that the learned deformation space generalizes well to the entire leaf base shapes.

First stage: Unlike existing skinned shape datasets [16, 26, 54] that provide the ground truth skinning weights and transformation matrices, our dataset is not synthetically generated and lacks the ground truth skinning parameters, i.e., we consider a correspondence-free case between the base and deformed shape. Therefore, we directly optimize

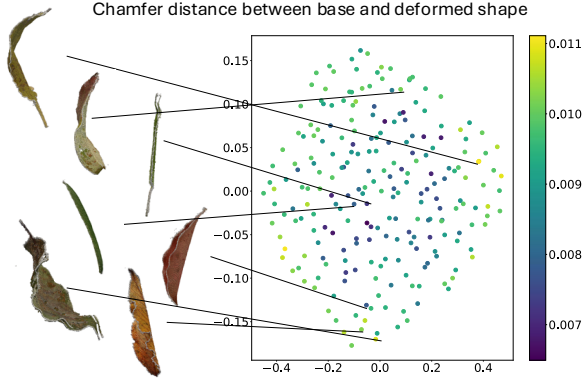


Figure 3. **Deformation mapping in the zero-mean latent space.** Samples closer to the center exhibit smaller deformations, while those farther from the center show greater deformations.

the chamfer distance between predicted deformed points $\bar{\mathcal{V}}$ and real points $\bar{\mathcal{V}}$ without any correspondence information. To ensure the smoothness of the leaf surface and to prevent undesired changes to the base shape, we incorporate several common regularizers: Mesh length loss $\mathcal{L}_{\text{leng}}$ penalizes large changes in the edge of \mathcal{S}_d to avoid drastic changes to the mesh geometry, and Laplacian smoothing loss \mathcal{L}_{lap} encourages smoothness of the surface by minimizing differences in local curvature. We also use a latent regularization term \mathcal{L}_{lat} defined similarly to Eq. (4), to constrain the latent space to a zero-mean Gaussian distribution.

Besides common constraints, we newly propose an additional regularization term, **deformation mapping loss** \mathcal{L}_{map} , to align the deformation latent space. Inspired by the fact that the deformation space forms a zero-mean Gaussian, we measure the chamfer distance d_{cham} between the base and deformed shape ($\mathcal{S}_b, \mathcal{S}_d$). The loss function maps the amount of deformation to the Gaussian distribution as

$$\mathcal{L}_{\text{map}} = \left(\frac{d_{\text{cham}}(\mathcal{S}_b, \mathcal{S}_d)}{\|\mathbf{z}_d\|_2} - \phi \right)^2, \quad (10)$$

so that the latent codes move away from zero as the chamfer distance increases, as visualized in Fig. 3. Here, ϕ is a learnable parameter that allows for an adaptable scaling factor that adjusts the penalization added by the chamfer distance on the latent code norm. The experiments show that the deformation space can be well trained on a relatively small dataset thanks to the disentangled latent spaces and the regularizers.

We minimize the losses over all D paired samples in DeformLeaf to optimize the deformation latent code $\{\mathbf{z}_d^i\}_{i=1}^D$, position of control points \mathcal{C} , decoder weights θ_d and θ_w as

$$\underset{\{\mathbf{z}_d^i\}, \mathcal{C}, \theta_w, \theta_d}{\text{argmin}} \sum_{i=1}^D (\mathcal{L}_{\text{cham}} + \mathcal{L}_{\text{leng}} + \mathcal{L}_{\text{lap}} + \mathcal{L}_{\text{map}} + \mathcal{L}_{\text{lat}}). \quad (11)$$

Second stage: The second stage aims to generalize the learned deformation space to the entire base shape space,

including those without explicitly paired deformation samples. Due to the significant differences between base shapes, minimizing the Chamfer distance between dissimilar leaf pairs without altering the base shape is challenging. We thus select m similar base shapes from the entire base shape space for each base shape in DeformLeaf based on the IoU between base masks, and we encourage similar base shapes to have similar skinning weights during training. We find that using only chamfer distance causes the unpaired base shape to overly conform to the deformed shape. We, therefore, introduce two additional boundary-focused constraints, **boundary length loss** $\mathcal{L}_{\text{bound}}$ and **face angle loss** \mathcal{L}_{ang} to maintain smoothness and preserve base shapes.

Boundary length loss aims to maintain the distance between adjacent contour vertices. We first extract contours of the base shape ψ . Contour vertices on the base shape \mathcal{S}_b is extracted as $\mathcal{V}'_c = \{\mathbf{v}' \in \mathcal{V}' \cap \psi\}$. Given the edge length between each pair of adjacent boundary vertices as $\|\mathbf{v}'_i - \mathbf{v}'_{i+1}\|_2$, boundary length loss $\mathcal{L}_{\text{bound}}$ is defined as

$$\mathcal{L}_{\text{bound}} = \sum_{\mathbf{v}' \in \mathcal{V}'} (\|\mathbf{v}'_i - \mathbf{v}'_{i+1}\|_2 - \|\mathbf{v}_i - \mathbf{v}_{i+1}\|_2)^2, \quad (12)$$

where $\mathbf{v}_i, \mathbf{v}_{i+1} \in \mathcal{V}$ represent the tentatively corresponding vertices in deformed shape \mathcal{S}_d varying during training.

Face angle loss encourages the angle around the contour vertices to become larger so that the boundaries will avoid sharp edges. For each boundary face $f_i \in \mathcal{F}_c$ containing a contour point \mathbf{v}_i , the connecting edges \mathbf{e}_1 and \mathbf{e}_2 form an angle $\theta(\mathbf{e}_1, \mathbf{e}_2)$, the face angle loss \mathcal{L}_{ang} is given by

$$\mathcal{L}_{\text{ang}} = \sum_{f_i \in \mathcal{F}_c} \frac{1}{\theta(\mathbf{e}_1, \mathbf{e}_2) + \epsilon}. \quad (13)$$

These two losses help to maintain the overall smoothness of the contour during the deformation process, focusing on the boundary points efficiently.

4. DeformLeaf Dataset

We construct a unique dataset of 3D deformed leaves and corresponding 2D base shapes. In the field of human modeling, 3D/4D human datasets typically include instances of subjects performing a variety of actions, each corresponding to a canonical pose. However, in our case, while some leaves undergo rapid deformations due to dehydration, they are often uncontrollable, making it challenging to capture the deformations within a controlled environment. This fact inspires us to disentangle the shape and deformation.

Dataset description Our DeformLeaf dataset comprises approximately 300 base-deformation leaf pairs, the capture setting is shown in Fig. 4. Multi-view images of a leaf are taken from various angles to gather comprehensive visual data, and a shot from a top-down view of the base image is

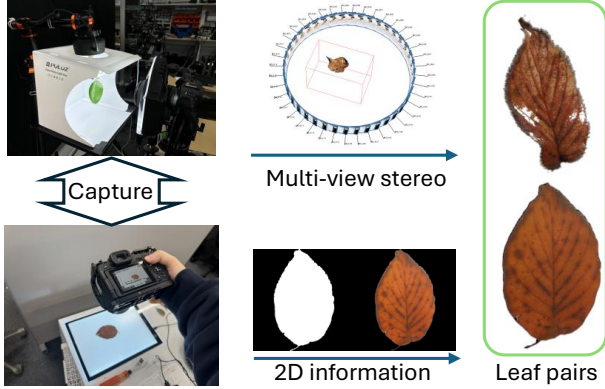


Figure 4. Pipeline of dataset acquisition.

also taken with a light board. The 3D reconstruction process is performed by Metashape¹.

Registration Although our NeuraLeaf does not require correspondences between the base and deformed shapes, we establish the dense correspondences in our dataset for experiments and future research. Our pipeline involves rigid registration followed by non-rigid registration, including As-Rigid-As-Possible (ARAP) [46] and the Coherent Point Drift (CPD) [10], which gradually relaxes the rigidity in registration. See supplementary materials for details.

5. NeuraLeaf Fitting to 3D Observations

Aside from pure CG modeling, NeuraLeaf can be used for reconstruction tasks by fitting our model to real-world observations. Especially in plant science and agriculture, beyond ordinary 3D shape reconstruction such as by multi-view stereo or RGB-D imaging, it is crucial to acquire 3D *structural* information such as topology, number, area, relationship, and direction of leaves from reconstructed shape information, in which our model helps.

We, therefore, provide a model fitting pipeline of NeuraLeaf to 3D shapes. The goal of NPM fitting is to find the set of latent codes, $(\mathbf{z}_s, \mathbf{z}_d)$ in our case, fit to the observations. To this end, our pipeline consists of the neural-net-based inversion of latent codes, followed by a direct optimization of the latent codes for refinement. We also take a similar fitting strategy for the texture latent \mathbf{z}_t but without the latent code inversion, which is detailed in the supplementary materials.

Preliminary: Input 3D shape representation We represent 3D shapes in SDF grids $\mathbf{G} \in \mathbb{R}^{D \times D \times D}$, providing a universal representation regardless of the input types (e.g., point clouds, mesh, and depth images). The individual leaf shapes are segmented by, such as existing segmentation methods [20], and roughly aligned using the rigid registration method described in Sec. 4.

¹Agisoft Metashape, <https://www.agisoft.com/>, last accessed on March 5, 2025.

Latent code inversion To obtain reasonable initialization of latent codes, we use an inversion-based approach inspired by [8]. Specifically, we train encoders using 3D convolutions, $(f_{\Omega_s}, f_{\Omega_d})$, which learn the mapping between the input SDF grid \mathbf{G} and the latent codes $(\mathbf{z}_s, \mathbf{z}_d)$ as

$$\mathbf{z}'_s = f_{\Omega_s}(\mathbf{G}), \quad \mathbf{z}'_d = f_{\Omega_d}(\mathbf{G}), \quad (14)$$

where $(\mathbf{z}'_s, \mathbf{z}'_d)$ are the inverted latent codes from the observations. The encoders are simply trained with the loss function \mathcal{L}_{inv} given by

$$\mathcal{L}_{inv} = \|\mathbf{z}'_s - \mathbf{z}_s\|_2^2 + \|\mathbf{z}'_d - \mathbf{z}_d\|_2^2. \quad (15)$$

Refinement by direct optimization Given the latent codes $(\mathbf{z}'_s, \mathbf{z}'_d)$ inferred by the encoders $(f_{\Omega_s}, f_{\Omega_d})$, we further optimize the latent codes to fit the observation. We compute the deformed shape \mathcal{S}'_d using the estimated latent codes $(\mathbf{z}'_s, \mathbf{z}'_d)$ and the pre-trained shape, skinning weight and transformation decoders $(f_{\theta_s}, f_{\theta_w}, f_{\theta_d})$. The latent codes are optimized to minimize the bi-directional chamfer loss $\mathcal{L}_{cham}(\mathcal{S}_d, \mathcal{S}'_d)$ with the regularization term \mathcal{L}_{reg} as the same manner in the training of MLPs $(f_{\theta_s}, f_{\theta_d})$ as

$$\mathcal{L}_{cham}(\mathcal{S}_d, \mathcal{S}'_d) = \quad (16)$$

$$\sum_{\mathbf{x} \in \mathcal{S}_d} \min_{\mathbf{x}' \in \mathcal{S}'_d} \|\mathbf{x}' - \mathbf{x}\|_2^2 + \sum_{\mathbf{x}' \in \mathcal{S}'_d} \min_{\mathbf{x} \in \mathcal{S}_d} \|\mathbf{x}' - \mathbf{x}\|_2^2,$$

$$\mathcal{L}_{reg} = \frac{\|\mathbf{z}_s\|_2^2}{\sigma_b^2} + \frac{\|\mathbf{z}_d\|_2^2}{\sigma_d^2}. \quad (17)$$

These loss functions are minimized through non-linear minimization using a gradient-descent method directly optimizing the latent codes $(\mathbf{z}'_s, \mathbf{z}'_d)$.

6. Experiments

We evaluate NeuraLeaf on modeling and reconstruction tasks from both quantitative and qualitative aspects. See supplementary materials for the implementation details.

6.1. Experiment Setup

Metrics To evaluate our reconstructions, we employed the ℓ_2 -Chamfer distance (C- ℓ_2) and normal consistency (NC). C- ℓ_2 [mm] is calculated between the closest point in the ground truth surface and the reconstructed surface, which evaluates point-wise discrepancies. Based on the closest correspondences, we calculate the normal consistency as the average cosine similarity between the surface normals of the ground truth and the estimated shapes.

Baselines We compare our NeuraLeaf with an existing parametric leaf model using PCA [5], a simplified version of the **B-spline**-based model [3, 12], and a straightforward extension of an existing human-oriented NPM [33] to leaves. Supplementary materials detail the implementations for the baseline methods.

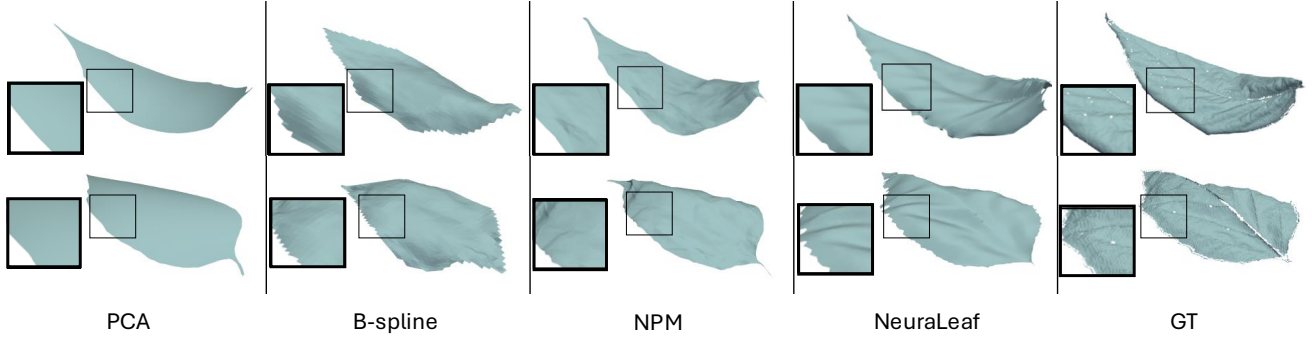


Figure 5. **Visual comparisons of reconstructed leaf samples.** We compare the ground truth with predicted shapes. Our method shows accurate reconstruction compared to baseline methods and has significantly more surface detail, such as leaf veins.

Table 1. **Quantitative comparison** between baselines on the test set of DeformLeaf dataset for single leaf reconstruction. The best result is highlighted in **bold**.

Method	$C\text{-}\ell_2$ [mm] ↓	NC ↑	Corres-free	Temp-free	Inf. time [s]
PCA [5]	32.7	0.924	×	×	157
B-spline [12]	26.7	0.957	✓	✓	18
NPM [33]	15.1	0.961	×	✓	73
NeuraLeaf (ours)	2.1	0.973	✓	✓	55

6.2. Results

Single leaf reconstruction Table 1 shows a quantitative comparison on fitting to real-world single-view partial leaf point clouds, which are the test set of DeformLeaf containing 30 leaves. Given the initial base shape estimated by the shape encoder f_{Ω_s} , the input point cloud is rigidly aligned to the base shape at first. According to the results, our NeuroLeaf outperforms the baseline methods, achieving higher normal consistency and also reducing chamfer distance, indicating that our proposed representation can benefit the reconstruction of the leaf surface. The visual comparisons in Fig. 5 confirm this tendency, where our method consistently achieves high-fidelity reconstruction.

Multiple leaf reconstruction To mimic practical use, we perform leaf reconstruction from observation of multiple leaves, which contain occlusions of leaves. We use top-view RGB-D observations of 5 plants, where we provide segmentation masks and obtain point clouds corresponding to each leaf instance. For the ground-truth shapes, we reconstruct the plants’ shapes by multi-view stereo (MVS) using many (≥ 100) images captured under a windless environment and to accurately recover the occlusions occurring in the top-view images. The fitting process for every single leaf employs the same workflow described in Sec. 5, while enhancing to share similar shape latent \mathbf{z}_s for the observation of the same plant species, whose details are described in the supplementary materials. For the NPM baseline, we also share the shape latent in a similar manner to our method.

Figure 6 presents a visual example of fitting multiple leaf instances to RGB-D observation, along with the quantitative comparisons summarized in Table 2. The leaf-wise

Table 2. **Quantitative results of multiple leaf reconstruction.**

Method	$C\text{-}\ell_2$ [mm] ↓	NC ↑
PCA [5]	1311.3	0.763
B-spline [12]	159.34	0.652
NPM [33] (sharing shape latent)	57.29	0.856
NeuraLeaf (w/o sharing)	117.14	0.681
NeuraLeaf (full model)	31.74	0.894

reconstruction results (see insets in Fig. 6) highlight that, by sharing similar shape latent \mathbf{z}_s , our method reasonably recovers leaf-wise shapes even in the portions occluded in the input RGB-D image. While the quantitative accuracies show an accurate reconstruction using our method, the visual examples highlight that NeuroLeaf reasonably recovers the hidden areas of leaves by sharing the shape latent among leaves. These results are promising for practical applications in agriculture, such as measuring the leaf areas.

Leaf modeling applications Beyond reconstruction, our NeuroLeaf can be used for CG applications of leaf shape generation through generation, interpolation, and transfer of latent codes. An example is illustrated in Fig. 7; sharing the same deformation latent code, we transform flat leaves into deformed leaves regardless of their base shapes. This highlights the merit of our learned disentanglement deformation representation, providing deformation consistency among different leaf species. These applications are beneficial in CG modeling, where leaves are often modeled as simple planes and usually lack detailed deformation. Refer to the supplementary materials and the video for other CG-related applications.

6.3. Ablation Study

Ablations of regularizer for deformation training We perform an ablation study to assess the effect of the deformation mapping loss \mathcal{L}_{map} used for the training of deformation space. Table 3 (top) shows the results of the ablation studies and demonstrates that deformation mapping loss contributes to the improvement of shape modeling.

Ablations of latent code inversion We also evaluate the ablation of latent code inversion using the encoders f_{Ω_s} and f_{Ω_d} as the initialization of latent codes for reconstruction

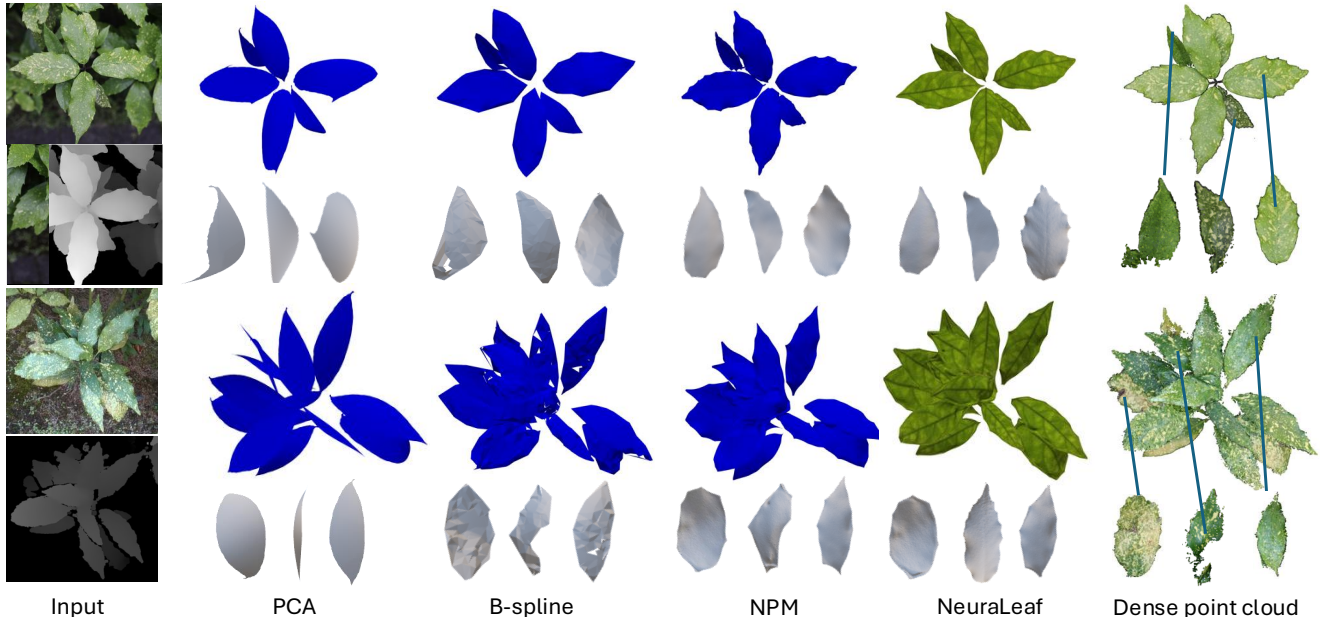


Figure 6. **Visual comparisons of multiple leaf reconstruction.** We use top-view RGB-D observations as input. Carefully captured multiview images are used to create the ground truths (denoted as “dense point cloud”). Our method achieves faithful reconstruction (*e.g.*, vein shapes on the leaf surfaces) and better occlusion recovery (*e.g.*, middle leaf in the bottom row).

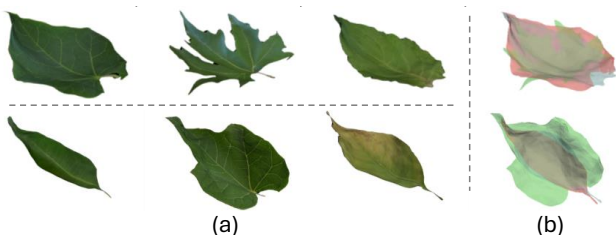


Figure 7. **Deformation transfer results.** Each row in (a) shows different leaf species with the same deformation latent. (b) demonstrate that each deformed leaf shape can be represented by a general surface, supporting the idea of a generalized deformation space capable of all kinds of leaf shapes.

Table 3. **Ablation studies.** We evaluate the chamfer distance-based regularization term \mathcal{L}_{map} , the latent code inversion using learned encoders, and the number of control points.

Method	$C\text{-}\ell_2$ [mm] ↓	NC ↑
w/o \mathcal{L}_{map}	5.3	0.971
w/o f_{Ω_s}	9.8	0.961
w/o f_{Ω_d}	14.7	0.934
# of control points	$C\text{-}\ell_2$ [mm] ↓	NC ↑
100 points	13.7	0.932
500 points	8.3	0.958
1000 points w/o optimization	21.4	0.954
Ours: NeuraLeaf (1000 points)	2.1	0.973

tasks. Specifically, we initialize the shape and deformation codes using the mean of the two spaces for the cases without these encoders. We observe that the quality of initialization by the latent code inversion significantly affects the fitting results, as shown in Table 3 (top).

Ablations of control points Since a unique characteristic of our method is using many control points, unlike NPMs for articulated objects, we conduct an ablation study on the number of control points. Table 3 (bottom) demonstrates that reducing the number of control points degrades the accuracy of reconstruction. Also, fixed (*i.e.*, w/o optimization of) control points significantly degrades the results.

7. Conclusions

This paper has presented NeuraLeaf, a novel leaf-specific NPM that faithfully captures the unique characteristics of leaf geometry. Our method effectively disentangles a leaf’s 3D structure into a 2D base shape and 3D deformation, each represented by a distinct latent code. By using large 2D-scanned image datasets and our newly acquired DeformLeaf dataset, NeuraLeaf learns from limited data while managing the flexibility inherent in leaf morphology. Through the experiments, we have shown that NeuraLeaf surpasses current traditional methods and NPMs in reconstructing leaf geometry. Also, the results show the capability of our model for real-world leaf-wise 3D reconstruction from RGB-D input. Our contributions offer a powerful tool for biological studies, CG, and related fields.

Limitations While NeuraLeaf shows promising results in reconstructing and generating leaf shapes, there are still limitations. First, due to the limited variety of leaf species in our DeformLeaf dataset, the model struggles to cover certain unique types of leaf deformations. Second, although we develop a texture space, optimizing the texture code to fit the target’s fine-grained appearance remains challenging.

NeuraLeaf: Neural Parametric Leaf Models with Shape and Deformation Disentanglement

Supplementary Material

In this supplementary material, we first provide details for our DeformLeaf dataset preparation and registration methods (Sec. A). We then provide more implementation details for training and evaluation, including the network architecture and implementation of the baseline methods (Sec. B), as well as details for model fitting (Sec. C).

Additional experimental settings and more qualitative results are shown in Sec. D and the supplementary video.

A. DeformLeaf Dataset Preparation

In this section, we detail the dataset preparation process, corresponding to Sec. 4 of the main paper. Our dataset, DeformLeaf, consists of approximately 300 base-deformation leaf pairs, where each pair contains both a 3D deformed shape and a 2D base shape with dense correspondences between them. First, we describe the extraction of the base shape from image masks in Sec. A.1. We also detail the rigid (Sec. A.2) and non-rigid (Sec. A.3) registration processes. Although our method, NeuraLeaf, itself does not rely on the dense correspondences between the base and deformed shape, we consider including the correspondence information in the DeformLeaf dataset facilitates baseline comparisons and supports future research.

A.1. Base Shape Extraction from Image Masks

Base shapes used in NeuraLeaf are extracted from 2D leaf image datasets. Given the mask region of leaves by an off-the-shelf segmentation method [20], we generate an SDF representation of base shapes for better compatibility with downstream tasks.

Specifically, we first calculate a 2D unsigned distance field (UDF) on the leaf’s plane (*i.e.*, $z = 0$ plane). Given an image mask, the UDF is first computed using the Jump Flooding algorithm (JFA) [41] on a 2D plane, which computes each pixel’s distance to the nearest object boundary. Then, the UDFs are post-processed to ensure the correct SDF sign and normalized against the maximum distance. As we described in the main paper, base shapes can be obtained in various representations by converting the 2D SDFs to other representations, such as meshes.

A.2. Rigid Registration

We first perform rigid registration for rough alignment between the base \mathcal{S}_b and deformed \mathcal{S}_d shapes. We take a similar but slightly different approach from the usual PCA-based alignment. The key to leaf pose estimation is to confirm the primary and secondary veins of the surface.

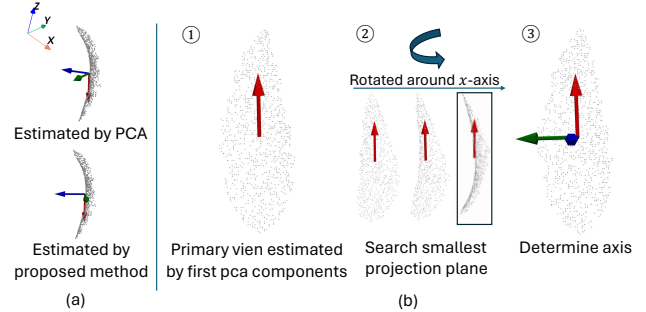


Figure S8. Rigid registration of deformed leaf shape \mathcal{S}_d .

Firstly, we compute the largest principal component of the vertices of the deformed shape to determine the primary vein (x -axis). Although conventional PCA-based alignment methods [30] use the second principal component as the secondary vein (y -axis), as leaf deformation increases, the shape variance around the secondary vein becomes large, as shown in Fig. S8(a). Instead, we seek the secondary vein (y -axis) as the direction perpendicular to the x -axis, where the projected area of the 3D shape is minimal, as in Fig. S8(b).

A.3. Non-rigid Registration

As mentioned in Sec. 4 in the main paper, we perform a non-rigid registration pipeline using the As-rigid-as-possible (ARAP) registration followed by the Coherent Point Drift (CPD) registration. Since the leaves have flexible deformation, it is often challenging to yield a reasonable registration by a single method. We, therefore, combine two registration methods to gradually relax the degrees of freedom in the deformation, namely, rigid alignment, ARAP assuming a locally rigid shape, and CPD as non-rigid registration.

As-rigid-as-possible (ARAP) registration In human and animal models, the deformations rely on their skeletal structures with hinged joints; *i.e.*, the deformation can be characterized as a rigid motion connected at joints. ARAP allows the model to bend or rotate around these joints while keeping the local shapes. Since leaves lack the hinged joints of the skeleton, we artificially designate the joint points (hereafter called keypoints) by uniformly sampling along both the base and the deformed leaves’ contour. By sampling the same number of points, we yield the correspondences between keypoints on the base shape and the scanned (*i.e.*, deformed) shapes.

Given the set of keypoints, $\mathcal{V} = \{\mathbf{v}_i \in \mathbb{R}^3\}_i$ and

$\mathcal{V}' = \{\mathbf{v}'_i \in \mathbb{R}^3\}_i$, defined on the base shape and deformed (*i.e.*, scanned) shape respectively, ARAP optimizes the vertex-specific offsets $\{\delta_i \in \mathbb{R}^3\}$ and rotation $\{\mathbf{R}_i \in \mathbb{R}^{3 \times 3}\}$. Specifically, we minimize the following energy function:

$$\sum_i \sum_{\mathbf{u} \in \mathcal{N}_{\mathbf{v}'_i}} (d(\hat{\mathbf{v}}_i - \mathbf{v}'_i) + \|(\hat{\mathbf{v}}_i - \hat{\mathbf{u}}) - \mathbf{R}_i(\mathbf{v}_i - \mathbf{u})\|_2^2), \quad (\text{S18})$$

where $\hat{\mathbf{v}}_i = \mathbf{v}_i + \delta_i$, $d(\hat{\mathbf{v}}_i - \mathbf{v}'_i)$ is the mean point-to-point distance from $\hat{\mathbf{v}}_i$ to its nearest neighbors in \mathcal{V}' , and $\mathcal{N}_{\mathbf{v}_i}$ denotes the nearest neighbouring vertices to \mathbf{v}_i .

Coherent point drift (CPD) registration We use a state-of-the-art implementation of CPD [10], which extends the original Euclidean CPD to non-Euclidean domains using the Laplace-Beltrami operator. This method addresses the challenge of a large search space using the nearest-neighbor descriptor matching to find confident correspondences. The probabilistic model of CPD is refined to manage outlier-contaminated initial correspondence sets effectively, employing an Expectation-Maximization (EM) approach for improved robustness and efficiency. See more details in [10].

B. Implementation Details

We train the NeuraLeaf model on a single RTX A6000 GPU using our DeformLeaf dataset. The dimensions of shape latent N_s , texture latent N_t , and deformation latent N_d are set to 256. For shape decoder f_{θ_s} , we apply the same architecture introduced in the Implicit Differentiable Renderer (IDR) [56] and train our models for 3,000 epochs. For the skinning decoder and transformation decoder, we use the network introduced in [54]. We use a learning rate of 10^{-3} for the networks and the latent codes. We implement a learning rate decay every 1,000 epochs. Similar to [33], latent inversion encoders ($f_{\Omega_s}, f_{\Omega_d}$) receive back-projected observation in the form of a partial SDF grid and output the latent code estimation through a series of 3D convolution layers and a final fully-connected layer. We hereafter detail the implementations further.

B.1. Architecture of Decoders

In this section, we provide an overview of the different networks used in our framework, each serving a specific role in capturing leaf shape, deformation, and texture. Specifically, our framework includes the following decoders: a **Shape decoder** f_{θ_s} for base shape representation, a **Texture generator** f_{θ_t} for modeling the leaf texture, a **Skinning Weights decoder** f_{θ_w} for predicting the influence weights of control points, and a **Transformation decoder** f_{θ_d} for calculating the transformations at each control point to achieve the desired deformation.

Shape decoder Shape decoder f_{θ_s} is an MLP that consists of 8 layers, with a dimension of hidden layers of 512 and a single skip connection from the input to the middle layer, which is similar to an existing NPM [8]. The initialization strategy of parameters of f_{θ_s} is the same as [2] so that f_{θ_s} produces an approximate SDF of a unit sphere.

Texture generator Similar to [58], the architecture of texture generator f_{θ_t} contains three convolution layers, multiple residual blocks, and two fractionally-strided convolution layers with stride $\frac{1}{2}$. We apply 9 blocks to 256×256 images and also use instance normalization. For the discriminator network, we apply a 70×70 PatchGAN to discriminate whether the overlapping image patches are real or fake.

Skinning weights decoder Skinning weights decoder f_{θ_w} uses the architecture introduced in [43], which is an MLP with intermediate layer shape (256, 256, 256, 1000) with a skip connection from the input feature to the 2nd layer, and non-linear activations using LeakyReLU except the last layer uses softmax layer to obtain normalized outputs. As input, we take the Cartesian coordinates of a base point sampled from base shape \mathcal{S}_b , which is encoded into a high-dimensional feature using positional encoding [39], incorporating up to 8th-order Fourier features.

Transformation decoder The transformation decoder f_{θ_d} follows a similar network architecture as the skinning weights decoder with an intermediate layer shape (256, 256, 256, 7), where the first four dimensions represent a quaternion for rotation and the remaining three dimensions represent translation. The input to the network consists of points sampled from the control points \mathcal{C} and also followed by positional encoding.

B.2. Training Details

We use Adam optimizer for f_{θ_s} , f_{θ_w} and f_{θ_d} and also apply a learning rate decay factor of 0.5 every 500 epochs. For training of base shape space, the SDF truncation is set to $\delta_\tau = 0.01$ and spherical covariance defined by σ_s is 10. For deformation latent codes, the spherical covariance defined by σ_d is also 10. Both shape latent codes $\{\mathbf{z}_s^i\}_{i=1}^S$ and deformation latent codes $\{\mathbf{z}_d^j\}_{j=1}^D$ are initialized randomly from $\mathcal{N}(0, 0.001)$.

B.3. Implementation of Baseline Methods

PCA-based parametric model [5] We evaluate the parametric leaf model proposed by Barley *et al.* [5]. This PCA-based approach needs dense correspondence among all shapes within the dataset. To accommodate this requirement, we partition our base shape dataset into several

groups based on shape characteristics. Each group’s shapes are registered to a template shape, then the parametric space is obtained based on BFM [36]. The template shapes are selected from DeformLeaf rather than using low-polygon leaf meshes, ensuring that the PCA baseline and other methods are compared at the same mesh resolution. For deformation modeling, we apply the same non-rigid fitting pipeline introduced in [5] and optimize the shape parameter simultaneously during inference.

Neural parametric model [33] We compare our method with a straightforward extension of the existing NPM [33], trained using our DeformLeaf dataset. Deformation modeling in this baseline is based on the neural displacement field. Thus, we use the dense correspondences in DeformLeaf for training. The training pipeline follows the paradigm in [33].

C. Model Fitting to 3D Observations

C.1. Details for Latent Code Inversion

As discussed in the main paper, we use two 3D convolutional networks f_{Ω_s} and f_{Ω_d} to map the back-projected SDF grid $\mathbf{G} \in \mathbb{R}^{128 \times 128 \times 128}$ to the initial latent code \mathbf{z}_s and \mathbf{z}_d at the inference stage. The convolutions are followed by a downsampling that creates growing receptive fields and channels with shrinking resolution, similar to common practices in 2D convolution. By applying this process recursively n times to input grid \mathbf{G} , it creates multi-scale deep feature grids $\{\mathbf{G}_1, \dots, \mathbf{G}_n\}$, each with a decreasing resolution $\mathbf{G}_k \in \mathbb{R}^{K \times K \times K}$, where $K = \frac{128}{2^{k-1}}$. Feature grids \mathbf{G}_k at early stages capture high frequencies, indicating fine shape details, whereas feature grids at later stages capture the global structure of the data.

C.2. Details for Direct Optimization

After initial latent code \mathbf{z}_s and \mathbf{z}_d predicted, we optimize for \mathbf{z}_s and \mathbf{z}_d by minimizing Eqs. (13) and (14) in the main paper. We use Adam optimizer and learning rate of 1×10^{-3} for both \mathbf{z}_s and \mathbf{z}_d . We optimize for a total of 300 iterations and perform learning rate decay by a factor of 0.5 every 50 iterations.

C.3. Texture Latent Estimation

In the limitation section of the main paper, we mention that our method has shortcomings in fitting the texture, as the texture latent code cannot be fitted to the input through fine-tuning. Therefore, we take the mean of the pre-trained texture space as the initial value, which is then updated.

C.4. Details for Multiple Leaf Reconstruction

To begin the reconstruction process, each leaf instance is initially processed by the shape encoder f_{Ω_s} to estimate the

Table S4. Additional ablation studies with $\mathcal{L}_{\text{bound}}$ and \mathcal{L}_{ang} .

Method	$C\text{-}\ell_2$ [mm] ↓	NC ↑
w/o $\mathcal{L}_{\text{bound}}$	9.4	0.971
w/o \mathcal{L}_{ang}	4.3	0.953
NeuraLeaf (full model)	2.1	0.973

shape latent code \mathbf{z}_s . However, due to occlusion or overlapping regions among leaves, some of the estimated shape codes might not accurately represent the true leaf shape. To identify a representative anchor latent code in the presence of potential outliers, we first compute the similarity between latent codes using Euclidean distance and perform clustering. Specifically, we employ K-means clustering to divide the latent codes into $K = 3$ clusters and select the cluster with the largest number of latent codes as the main cluster, assuming that this cluster represents the normal shape. Once the main cluster is identified, we choose an anchor latent code $\mathbf{z}_s^{\text{anc}}$, by selecting the code closest to the cluster center. $\mathbf{z}_s^{\text{anc}}$ serves as the reference during optimization. Formally, we introduce a regularization term \mathcal{L}_{anc} defined as

$$\mathcal{L}_{\text{anc}} = \|\mathbf{z}_s - \mathbf{z}_s^{\text{anc}}\|_2, \quad (\text{S19})$$

ensuring that the shape latent codes for each leaf instance do not deviate significantly from the reference shape.

D. More Results and Analysis

We also strongly encourage readers to refer to the supplementary video for more intuitive visualizations.

Shape interpolation We show interpolation results between base shapes with distinct differences in Fig. S9, showing the smoothness and compactness of our base latent space, which is useful for CG leaf shape modeling using NeuraLeaf.

More generation examples We also show different samples in the same deformation pattern (*i.e.*, deformed by the same deform code \mathbf{z}_d) in Fig. S10, to evaluate the deformation consistency among different base leaf shapes.

Visualization of skinning weights We also show the results of interpolating shape codes with fixed deformation in Fig. S11 along with their skinning weights. Although skinning weights are shape-dependent, they are mostly consistent across base shapes, allowing the model to adapt to unseen leaf shapes.

Random shape generation NeuraLeaf also allows the leaf shape generation by random sampling in the shape space, as shown in Fig. S12, showing that the shape latent is reasonably constructed.

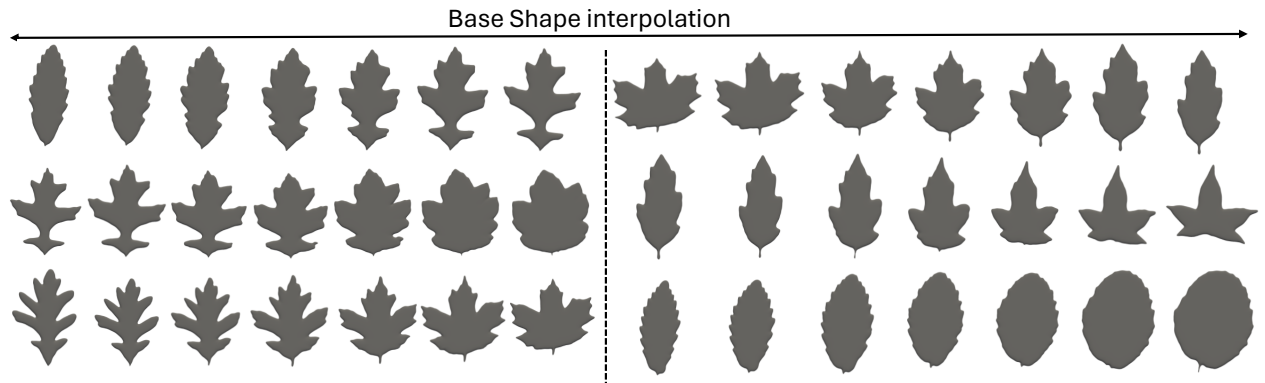


Figure S9. Interpolation between diverse base shapes, showing the smoothness of our base shape latent space.

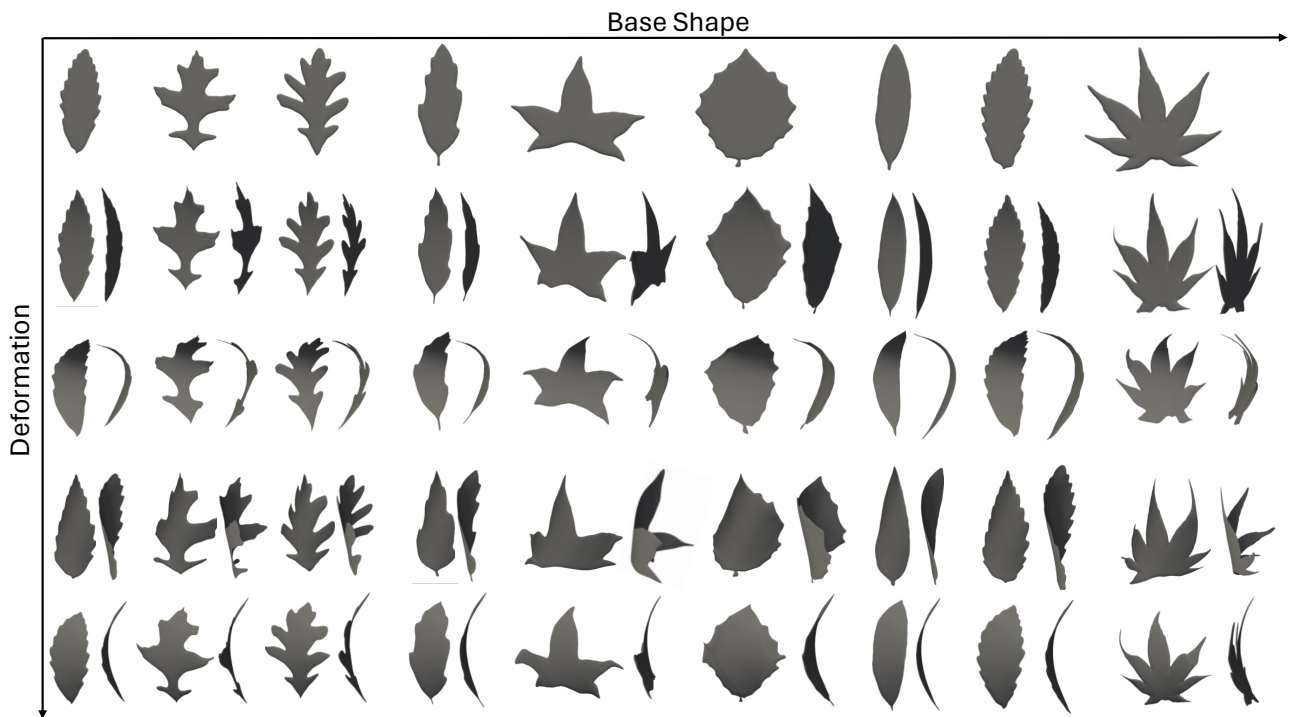


Figure S10. Deformation among different kinds of base shapes. Each row shows the results using the same deformation latent codes.

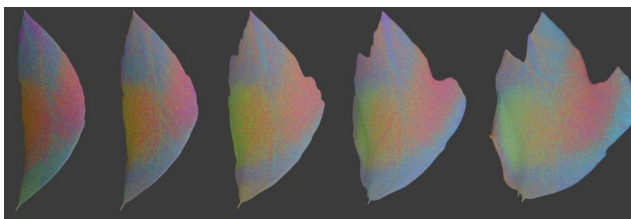


Figure S11. Visualization of skinning weights during shape interpolation.



Figure S12. Shape generation via random sampling of shape latent.

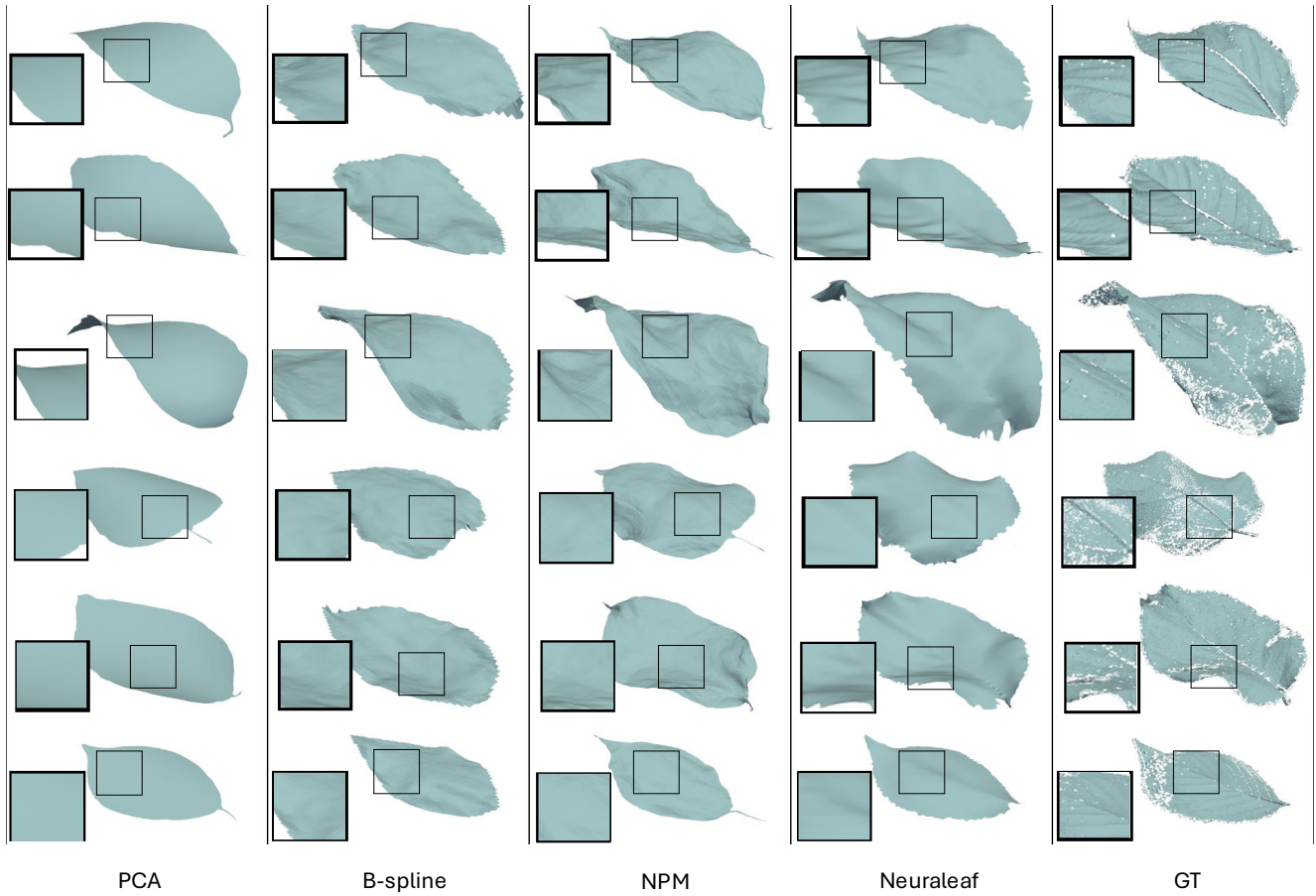


Figure S13. Additional comparison of single-leaf reconstruction.

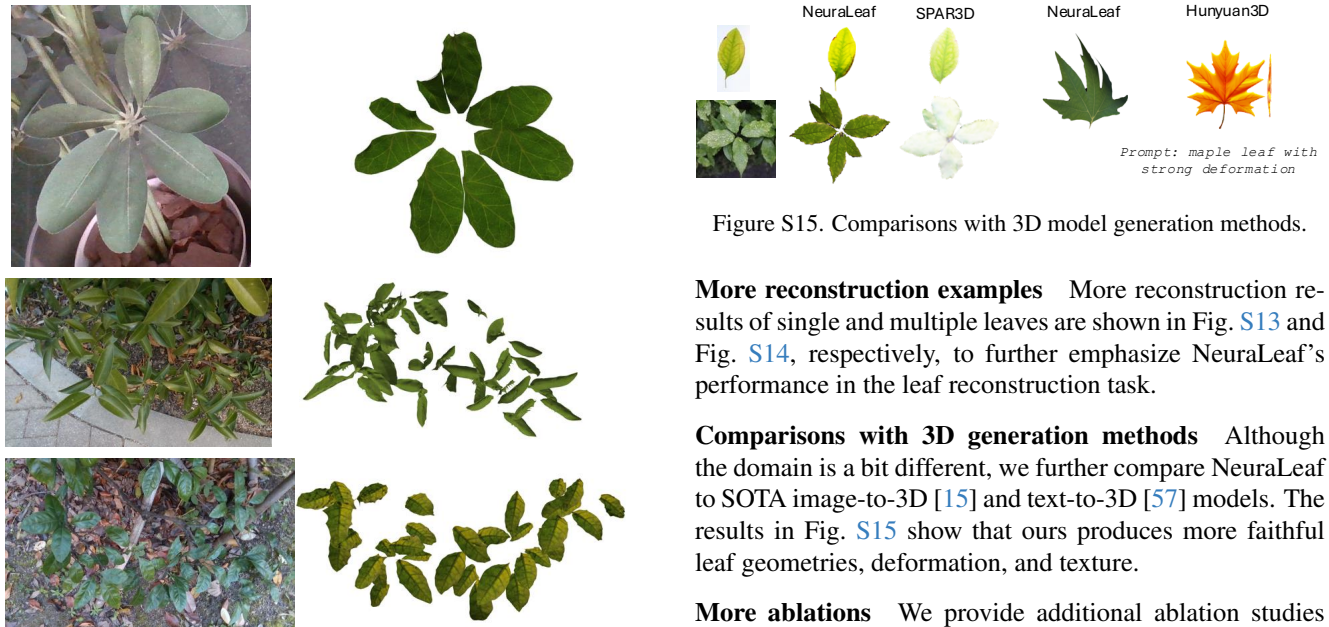


Figure S14. Additional result of multiple leaf reconstruction.

Figure S15. Comparisons with 3D model generation methods.

More reconstruction examples More reconstruction results of single and multiple leaves are shown in Fig. S13 and Fig. S14, respectively, to further emphasize NeuraLeaf’s performance in the leaf reconstruction task.

Comparisons with 3D generation methods Although the domain is a bit different, we further compare NeuraLeaf to SOTA image-to-3D [15] and text-to-3D [57] models. The results in Fig. S15 show that ours produces more faithful leaf geometries, deformation, and texture.

More ablations We provide additional ablation studies specifically targeting boundary length loss and face angle loss in Table S4, demonstrating that they can help avoid overfitting to local optima.

Acknowledgments

This work was supported in part by the JSPS KAKENHI JP23H05491, JP25K03140, and JST FOREST JP-MJFR206F.

References

- [1] Dragomir Anguelov, Praveen Srinivasan, Daphne Koller, Sebastian Thrun, Jim Rodgers, and James Davis. SCAPE: Shape completion and animation of people. *ACM Transactions on Graphics (TOG)*, 24(3):408–416, 2005. 2
- [2] Matan Atzmon and Yaron Lipman. SAL: Sign agnostic learning of shapes from raw data. In *Proceedings of IEEE/CVF Conference on Computer Vision and Pattern Recognition (CVPR)*, 2020. 10
- [3] Paul Beardsley and Gaurav Chaurasia. Editable parametric dense foliage from 3D capture. In *Proceedings of IEEE/CVF International Conference on Computer Vision (ICCV)*, 2017. 1, 2, 6
- [4] Volker Blanz and Thomas Vetter. A morphable model for the synthesis of 3D faces. In *Proceedings of ACM Annual Conference on Computer Graphics and Interactive Techniques (SIGGRAPH)*, 1999. 2
- [5] Derek Bradley, Derek Nowrouzezahrai, and Paul Beardsley. Image-based reconstruction and synthesis of dense foliage. *ACM Transactions on Graphics (TOG)*, 32(4):74:1–74:10, 2013. 1, 2, 6, 7, 10, 11
- [6] Christoph Bregler, Aaron Hertzmann, and Henning Biermann. Recovering non-rigid 3D shape from image streams. In *Proceedings of IEEE/CVF Conference on Computer Vision and Pattern Recognition (CVPR)*, 2000. 2
- [7] Xu Chen, Yufeng Zheng, Michael J Black, Otmar Hilliges, and Andreas Geiger. SNARF: Differentiable forward skinning for animating non-rigid neural implicit shapes. In *Proceedings of IEEE/CVF International Conference on Computer Vision (ICCV)*, 2021. 1
- [8] Julian Chibane, Thiemo Alldieck, and Gerard Pons-Moll. Implicit functions in feature space for 3D shape reconstruction and completion. In *Proceedings of IEEE/CVF Conference on Computer Vision and Pattern Recognition (CVPR)*, 2020. 6, 10
- [9] Siddharth Singh Chouhan, Ajay Kaul, Uday Pratap Singh, and Sanjeev Jain. A data repository of leaf images: Practice towards plant conservation with plant pathology. In *Proceedings of International Conference on Information Systems and Computer Networks (ISCON)*, 2019. 3
- [10] Aoxiang Fan, Jiayi Ma, Xin Tian, Xiaoguang Mei, and Wei Liu. Coherent point drift revisited for non-rigid shape matching and registration. In *Proceedings of IEEE/CVF Conference on Computer Vision and Pattern Recognition (CVPR)*, 2022. 6, 10
- [11] Simon Giebenhain, Tobias Kirschstein, Markos Georgopoulos, Martin Rünz, Lourdes Agapito, and Matthias Nießner. Learning neural parametric head models. In *Proceedings of IEEE/CVF Conference on Computer Vision and Pattern Recognition (CVPR)*, 2023. 1, 2
- [12] William J. Gordon and Richard F. Riesenfeld. B-spline curves and surfaces. *Computer Aided Geometric Design*, 1974:95–126, 1974. 6, 7
- [13] Amos Gropp, Lior Yariv, Niv Haim, Matan Atzmon, and Yaron Lipman. Implicit geometric regularization for learning shapes. In *Proceedings of International Conference on Machine Learning (ICML)*, 2020. 4
- [14] Sung Min Hong. Shape modeling of plant leaves with unstructured meshes. Master’s thesis, University of Waterloo, 2005. 3
- [15] Zixuan Huang, Mark Boss, Aaryaman Vasishta, James M Rehg, and Varun Jampani. SPAR3D: Stable point-aware reconstruction of 3D objects from single images. *arXiv preprint arXiv:2501.04689*, 2025. 13
- [16] Catalin Ionescu, Dragos Papava, Vlad Olaru, and Cristian Sminchisescu. Human3.6M: Large scale datasets and predictive methods for 3D human sensing in natural environments. *IEEE Transactions on Pattern Analysis and Machine Intelligence (PAMI)*, 36(7):1325–1339, 2014. 4
- [17] Alec Jacobson, Zhigang Deng, Ladislav Kavan, and JP Lewis. Skinning: Real-time shape deformation. In *ACM SIGGRAPH 2014 Courses*, 2014. 3, 4
- [18] Jacek Kafuzny, Yannik Schreckenberg, Karol Cyganik, Peter Annighöfer, Sören Pirk, Dominik L Michels, Mikolaj Cieslak, Farhah Assaad-Gerber, Bedrich Benes, and Wojciech Patubicki. LAESI: Leaf area estimation with synthetic imagery. *arXiv preprint arXiv:2404.00593*, 2024. 1
- [19] Daeyeoul Kim and Jinmo Kim. Procedural modeling and visualization of multiple leaves. *Multimedia Systems*, 23: 435–449, 2017. 2
- [20] Alexander Kirillov, Eric Mintun, Nikhila Ravi, Hanzi Mao, Chloe Rolland, Laura Gustafson, Tete Xiao, Spencer Whitehead, Alexander C Berg, Wan-Yen Lo, et al. Segment anything. In *Proceedings of IEEE/CVF International Conference on Computer Vision (ICCV)*, 2023. 3, 6, 9
- [21] Chen Kong and Simon Lucey. Deep non-rigid structure from motion. In *Proceedings of IEEE/CVF International Conference on Computer Vision (ICCV)*, 2019. 2
- [22] Tianye Li, Timo Bolkart, Michael J. Black, Hao Li, and Javier Romero. Learning a model of facial shape and expression from 4D scans. *ACM Transactions on Graphics (TOG)*, 36(6):194:1–194:17, 2017. 2
- [23] Matthew Loper, Naureen Mahmood, Javier Romero, Gerard Pons-Moll, and Michael J. Black. SMPL: A skinned multi-person linear model. *ACM Transactions on Graphics (TOG)*, 34(6):248:1–248:16, 2015. 1, 2
- [24] Shenglian Lu, Chunjiang Zhao, and Xinyu Guo. Venation skeleton-based modeling plant leaf wilting. *International Journal of Computer Games Technology*, 2009:890917:1–890917:8, 2009. 3
- [25] Qianli Ma, Jinlong Yang, Anurag Ranjan, Sergi Pujades, Gerard Pons-Moll, Siyu Tang, and Michael J. Black. Learning to dress 3D people in generative clothing. In *Proceedings of IEEE/CVF Conference on Computer Vision and Pattern Recognition (CVPR)*, 2020. 2
- [26] Naureen Mahmood, Nima Ghorbani, Nikolaus F. Troje, Gerard Pons-Moll, and Michael J. Black. AMASS: Archive

- of motion capture as surface shapes. In *Proceedings of IEEE/CVF International Conference on Computer Vision (ICCV)*, 2019. 4
- [27] Teng Miao, ChunJiang Zhao, XinYu Guo, and ShengLian Lu. A framework for plant leaf modeling and shading. *Mathematical and Computer Modelling*, 58(3-4):710–718, 2013. 2
- [28] Marko Mihajlovic, Yan Zhang, Michael J Black, and Siyu Tang. LEAP: Learning articulated occupancy of people. In *Proceedings of IEEE/CVF Conference on Computer Vision and Pattern Recognition (CVPR)*, 2021. 2
- [29] Ben Mildenhall, Pratul P Srinivasan, Matthew Tancik, Jonathan T Barron, Ravi Ramamoorthi, and Ren Ng. NeRF: Representing scenes as neural radiance fields for view synthesis. In *Proceedings of European Conference on Computer Vision (ECCV)*, 2020. 1
- [30] Gunjan Mukherjee, Arpitam Chatterjee, and Bipan Tudu. Morphological feature based maturity level identification of kalmegh and tulsi leaves. In *Proceedings of International Conference on Research in Computational Intelligence and Communication Networks (ICRCICN)*, 2017. 9
- [31] Thomas Müller, Alex Evans, Christoph Schied, and Alexander Keller. Instant neural graphics primitives with a multi-resolution hash encoding. *ACM Transactions on Graphics (TOG)*, 41(4):102:1–102:15, 2022. 1
- [32] Michael Niemeyer, Lars Mescheder, Michael Oechsle, and Andreas Geiger. Occupancy flow: 4D reconstruction by learning particle dynamics. In *Proceedings of IEEE/CVF International Conference on Computer Vision (ICCV)*, 2019. 2
- [33] Pablo Palafox, Aljaž Božič, Justus Thies, Matthias Nießner, and Angela Dai. NPMs: Neural parametric models for 3D deformable shapes. In *Proceedings of IEEE/CVF International Conference on Computer Vision (ICCV)*, 2021. 1, 2, 4, 6, 7, 10, 11
- [34] Pablo Palafox, Nikolaos Sarafianos, Tony Tung, and Angela Dai. SPAMs: Structured implicit parametric models. In *Proceedings of IEEE/CVF Conference on Computer Vision and Pattern Recognition (CVPR)*, 2022. 1, 2
- [35] Jeong Joon Park, Peter Florence, Julian Straub, Richard Newcombe, and Steven Lovegrove. DeepSDF: Learning continuous signed distance functions for shape representation. In *Proceedings of IEEE/CVF Conference on Computer Vision and Pattern Recognition (CVPR)*, 2019. 2
- [36] Pascal Paysan, Reinhard Knothe, Brian Amberg, Sami Romdhani, and Thomas Vetter. A 3D face model for pose and illumination invariant face recognition. In *Proceedings of IEEE International Conference on Advanced Video and Signal Based Surveillance (AVSS)*, 2009. 11
- [37] Sida Peng, Junting Dong, Qianqian Wang, Shangzhan Zhang, Qing Shuai, Xiaowei Zhou, and Hujun Bao. Animatable neural radiance fields for modeling dynamic human bodies. In *Proceedings of IEEE/CVF International Conference on Computer Vision (ICCV)*, 2021. 1
- [38] Gerard Pons-Moll, Javier Romero, Mahmood Naureen, and Michael J. Black. Dyna: A model of dynamic human shape in motion. *ACM Transactions on Graphics (TOG)*, 34(4):120:1–120:14, 2015. 2
- [39] Nasim Rahaman, Aristide Baratin, Devansh Arpit, Felix Draxler, Min Lin, Fred Hamprecht, Yoshua Bengio, and Aaron Courville. On the spectral bias of neural networks. In *Proceedings of International Conference on Machine Learning (ICML)*, 2019. 10
- [40] Javier Romero, Dimitrios Tzionas, and Michael J. Black. Embodied hands: Modeling and capturing hands and bodies together. *ACM Transactions on Graphics (TOG)*, 36(6):245:1–245:17, 2017. 2
- [41] Guodong Rong and Tiow-Seng Tan. Jump flooding in GPU with applications to voronoi diagram and distance transform. In *Proceedings of Symposium on Interactive 3D Graphics and Games (I3D)*, 2006. 9
- [42] Adam Runions, Martin Fuhrer, Brendan Lane, Pavol Federl, Anne-Gaëlle Rolland-Lagan, and Przemyslaw Prusinkiewicz. Modeling and visualization of leaf venation patterns. *ACM Transactions on Graphics (TOG)*, 24(3):702–711, 2005. 1, 3
- [43] Shunsuke Saito, Jinlong Yang, Qianli Ma, and Michael J Black. SCANimate: Weakly supervised learning of skinned clothed avatar networks. In *Proceedings of IEEE/CVF Conference on Computer Vision and Pattern Recognition (CVPR)*, 2021. 10
- [44] Uday Pratap Singh Siddharth Singh Chouhan, Ajay Kaul and Sanjeev Jain. A database of leaf images: Practice towards plant conservation with plant pathology. In *Proceedings of International Conference on Information Systems and Computer Networks (ISCON)*, 2019. 1
- [45] Jeong Sohyeon, Si-Hyung Park, and Chang-Hun Kim. Simulation of morphology changes in drying leaves. *Computer Graphics Forum*, 32(1):204–215, 2013. 3
- [46] Olga Sorkine and Marc Alexa. As-rigid-as-possible surface modeling. In *Proceedings of Eurographics Symposium on Geometry Processing (SGP)*, 2007. 2, 6
- [47] Garvita Tiwari, Bharat Lal Bhatnagar, Tony Tung, and Gerard Pons-Moll. SIZER: A dataset and model for parsing 3D clothing and learning size sensitive 3D clothing. In *Proceedings of European Conference on Computer Vision (ECCV)*, 2020. 2
- [48] Shubham Tulsiani, Nilesh Kulkarni, and Abhinav Gupta. Implicit mesh reconstruction from unannotated image collections. *arXiv preprint arXiv:2007.08504*, 2020. 2
- [49] Lizhen Wang, Zhiyuan Chen, Tao Yu, Chenguang Ma, Liang Li, and Yebin Liu. FaceVerse: A fine-grained and detail-controllable 3D face morphable model from a hybrid dataset. In *Proceedings of IEEE/CVF Conference on Computer Vision and Pattern Recognition (CVPR)*, 2022. 2
- [50] Peng Wang, Lingjie Liu, Yuan Liu, Christian Theobalt, Taku Komura, and Wenping Wang. NeuS: Learning neural implicit surfaces by volume rendering for multi-view reconstruction. In *Advances in Neural Information Processing Systems (NeurIPS)*, 2021. 1
- [51] Weiliang Wen, Baojun Li, Bao-jun Li, and Xinyu Guo. A leaf modeling and multi-scale remeshing method for visual computation via hierarchical parametric vein and margin representation. *Frontiers in Plant Science*, 9(783), 2018. 1, 3

- [52] Shangzhe Wu, Ruining Li, Tomas Jakab, Christian Rupprecht, and Andrea Vedaldi. MagicPony: Learning articulated 3D animals in the wild. In *Proceedings of IEEE/CVF Conference on Computer Vision and Pattern Recognition (CVPR)*, 2023. [2](#)
- [53] Yuefan Wu, Zeyuan Chen, Shaowei Liu, Zhongzheng Ren, and Shenlong Wang. CASA: Category-agnostic skeletal animal reconstruction. In *Advances in Neural Information Processing Systems (NeurIPS)*, 2022. [2](#)
- [54] Zhan Xu, Yang Zhou, Evangelos Kalogerakis, Chris Landreth, and Karan Singh. RigNet: Neural rigging for articulated characters. *ACM Transactions on Graphics (TOG)*, 39(4):58:1–58:14, 2020. [4](#), [10](#)
- [55] Chun-Han Yao, Wei-Chih Hung, Yuanzhen Li, Michael Rubinstein, Ming-Hsuan Yang, and Varun Jampani. Hiclassie: High-fidelity articulated shape and skeleton discovery from sparse image ensemble. In *Proceedings of IEEE/CVF Conference on Computer Vision and Pattern Recognition (CVPR)*, 2023. [2](#)
- [56] Lior Yariv, Yoni Kasten, Dror Moran, Meirav Galun, Matan Atzmon, Basri Ronen, and Yaron Lipman. Multiview neural surface reconstruction by disentangling geometry and appearance. In *Advances in Neural Information Processing Systems (NeurIPS)*, 2020. [10](#)
- [57] Zibo Zhao, Zeqiang Lai, Qingxiang Lin, Yunfei Zhao, Haolin Liu, Shuhui Yang, Yifei Feng, Mingxin Yang, Sheng Zhang, Xianghui Yang, et al. Hunyuan3D 2.0: Scaling diffusion models for high resolution textured 3D assets generation. *arXiv preprint arXiv:2501.12202*, 2025. [13](#)
- [58] Jun-Yan Zhu, Taesung Park, Phillip Isola, and Alexei A Efros. Unpaired image-to-image translation using cycle-consistent adversarial networks. In *Proceedings of IEEE/CVF International Conference on Computer Vision (ICCV)*, 2017. [4](#), [10](#)
- [59] Silvia Zuffi, Angjoo Kanazawa, David Jacobs, and Michael J. Black. 3D menagerie: Modeling the 3D shape and pose of animals. In *Proceedings of IEEE/CVF Conference on Computer Vision and Pattern Recognition (CVPR)*, 2017. [1](#), [2](#)